Supporting Information

Built-in tensile strain dependence on lateral size of monolayer MoS_2 using liquid precursor chemical vapor deposition

L. Seravalli[1], F. Esposito[1,2], M. Bosi[1], L. Aversa[3], G. Trevisi[1], R. Verucchi[3], L. Lazzarini[1], F. Rossi[1], F. Fabbri[4]

[1] Institute of Materials for Electronics and Magnetism (IMEM-CNR), Parco Area delle Scienze 37/a, 43124 Parma, Italy

[2] Department of Mathematical, Physical and Computer Sciences, University of Parma, Parco Area delle Scienze 7/a, 43124 Parma, Italy

[3] Institute of Materials for Electronics and Magnetism (IMEM-CNR), FBK Trento unit, Via alla Cascata 56/C, 38123 Povo (Trento), Italy

[4] NEST, Istituto Nanoscienze – CNR, Scuola Normale Superiore, Piazza San Silvestro 12, 56127 Pisa, Italy

List of the Figures:

Figure S1: Cross-sectional TEM analysis of 830°C grown MoS_2 ML.

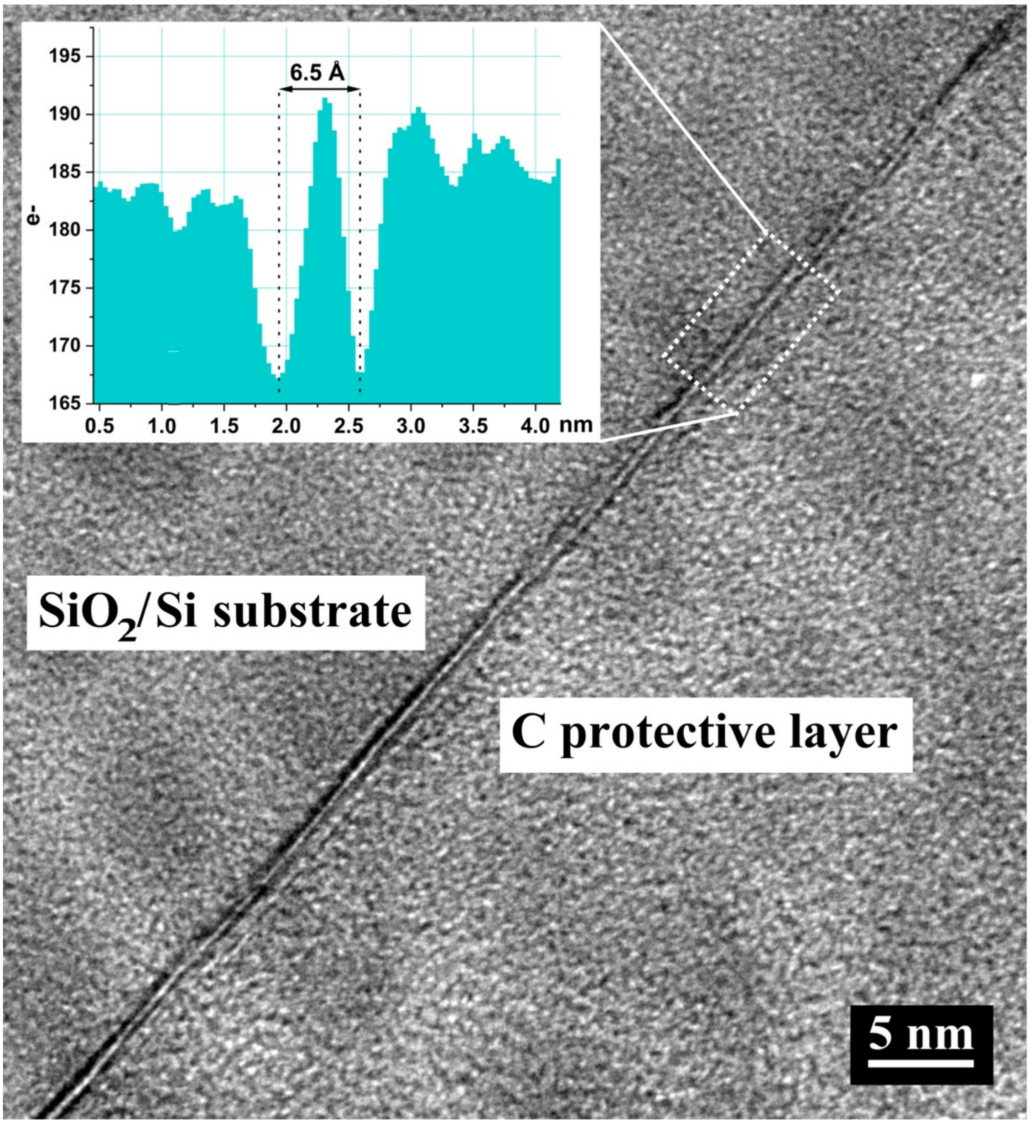

Fig. S1. A representative TEM image acquired at the interface, where MoS_2 is embedded between the amorphous SiO_2 and the protective Carbon coating. As shown from the intensity profile in the inset, a layer thickness of 0.65 nm is measured, that corresponds to the characteristic monolayer thickness of MoS_2.

S2 Statistical analysis of the nanoparticles morphology

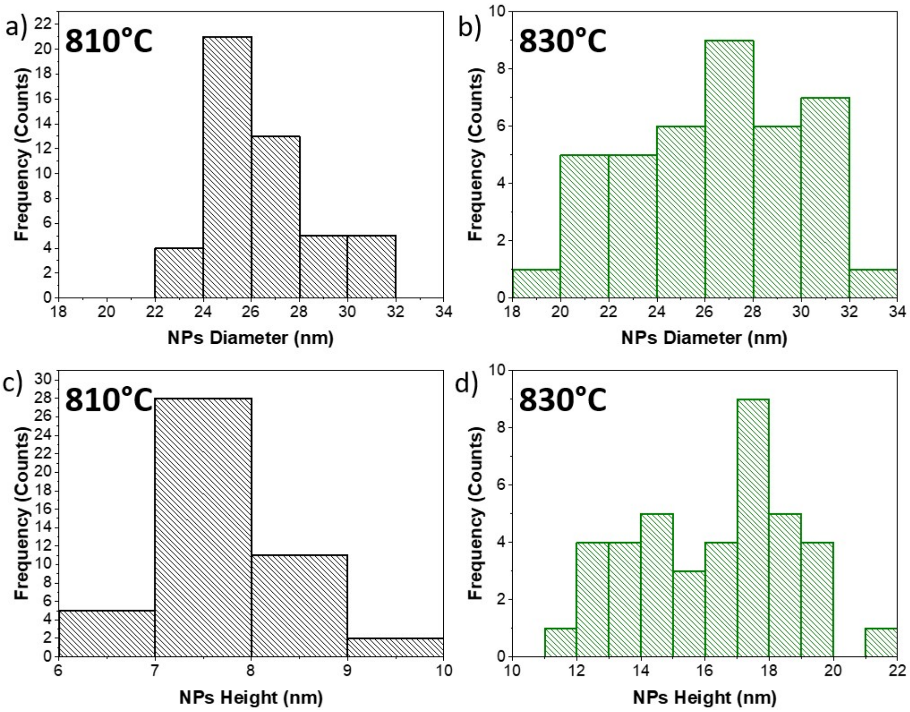

Fig. S2 a), b) histogram of the NP diameter in case of the 810°C and 830°C synthetized MLs. c) and d) histogram of the NP height in case of the 810°C and 830°C synthetized MLs.

Histogram presents the statistical analysis of the NP size decorating the edge of the ML edge. Fig S2 a) and b) show the NPs diameter of ML grown at 810°C and 830°C, obtained by the AFM mapping reported in Fig. 2. While Fig. 2 c) an d) present the histograms of the NP height ML grown at 810°C and 830°C.

Figure S3: Raman mapping and optical microscopy of the MoS_2 mode separation and of the intensity of the E_{2g} mode.

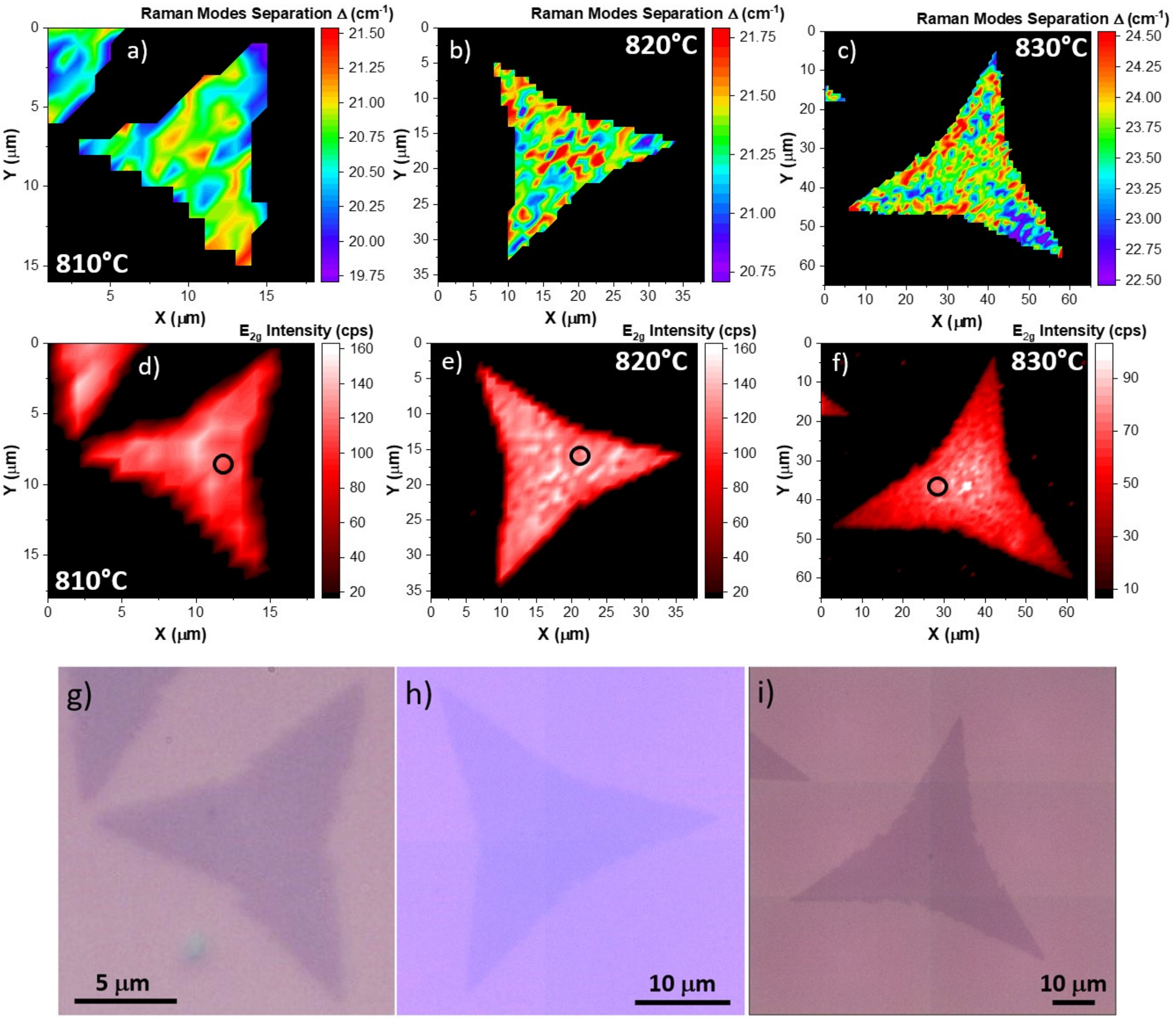

Fig. S3 a), b) and c) Raman modes separation maps of the MoS_2 ML grown at 810°C, 820°C and 830°C, respectively. d), e) and f) E_{2g} intensity maps of the MoS_2 ML grown at 810°C, 820°C and 830°C, respectively. The black rings indicate where the spectra of Fig. 3 a are collected. g), h), and i) optical microscopy micrographs of the MoS_2 ML grown at 810°C, 820°C and 830°C, respectively.

The Raman mode separation maps reveal an enhanced mode separation, with increasing the growth temperature, as reported in Fig (S3a, S3b and S3c). The data reported here are employed for the statistical study shown in Fig. 3b. The intensity of the E_{2g} mode are shown in Fig S3d, S3e and S3f for increasing growth temperature. The main effect is reported in Fig. S3f where the intensity of the E_{2g} mode appears fainter in the vertexes of the triangular structure, an effect that can be related to the presence of defects, as the nanocracks reported in Fig. 4b. The optical micrographs of the MoS_2 MLs obtained at increasing temperature (panel g), h) and i)), showing no optical contrast inside the MLs, suggesting a homogeneous thickness, for all the different growth temperatures.

Figure S3: Raman spectra in the range of the amorphous carbon.

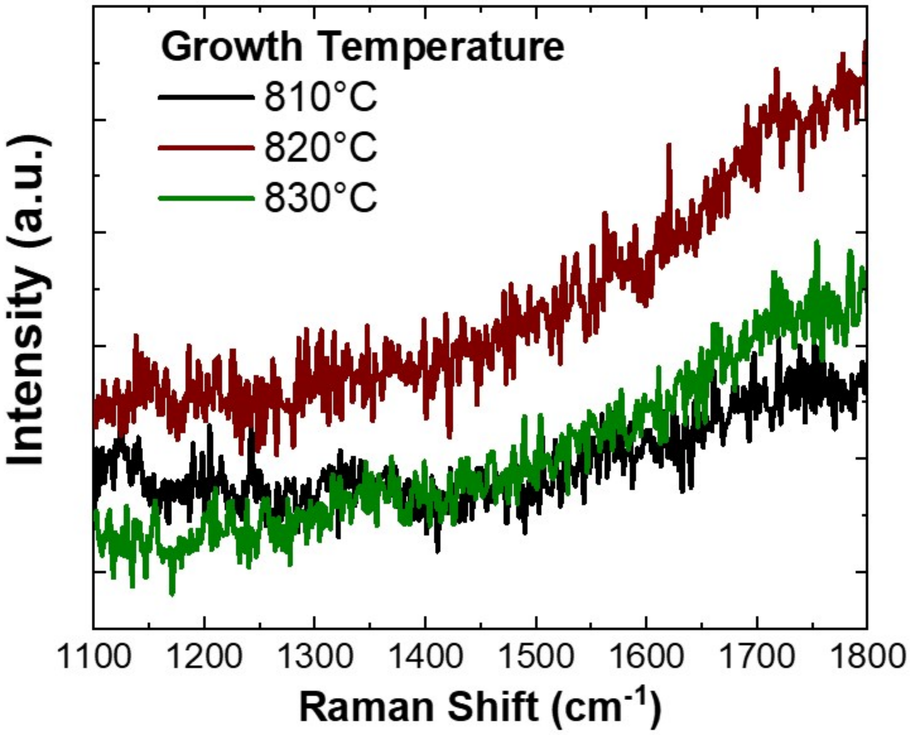

Fig. S4 Raman spectra of the MoS_2 MLs grown at increasing temperature in the range of amorphous carbon.

The Raman spectra in the range of amorphous carbon reveal no peaks that can be assigned to the presence of amorphous carbon in all the specimens in analysis. This result was previously reported for similar CVD process.[1]

Figure S5: Transfer process and characterization of the MoS_2 MLs after transfer.

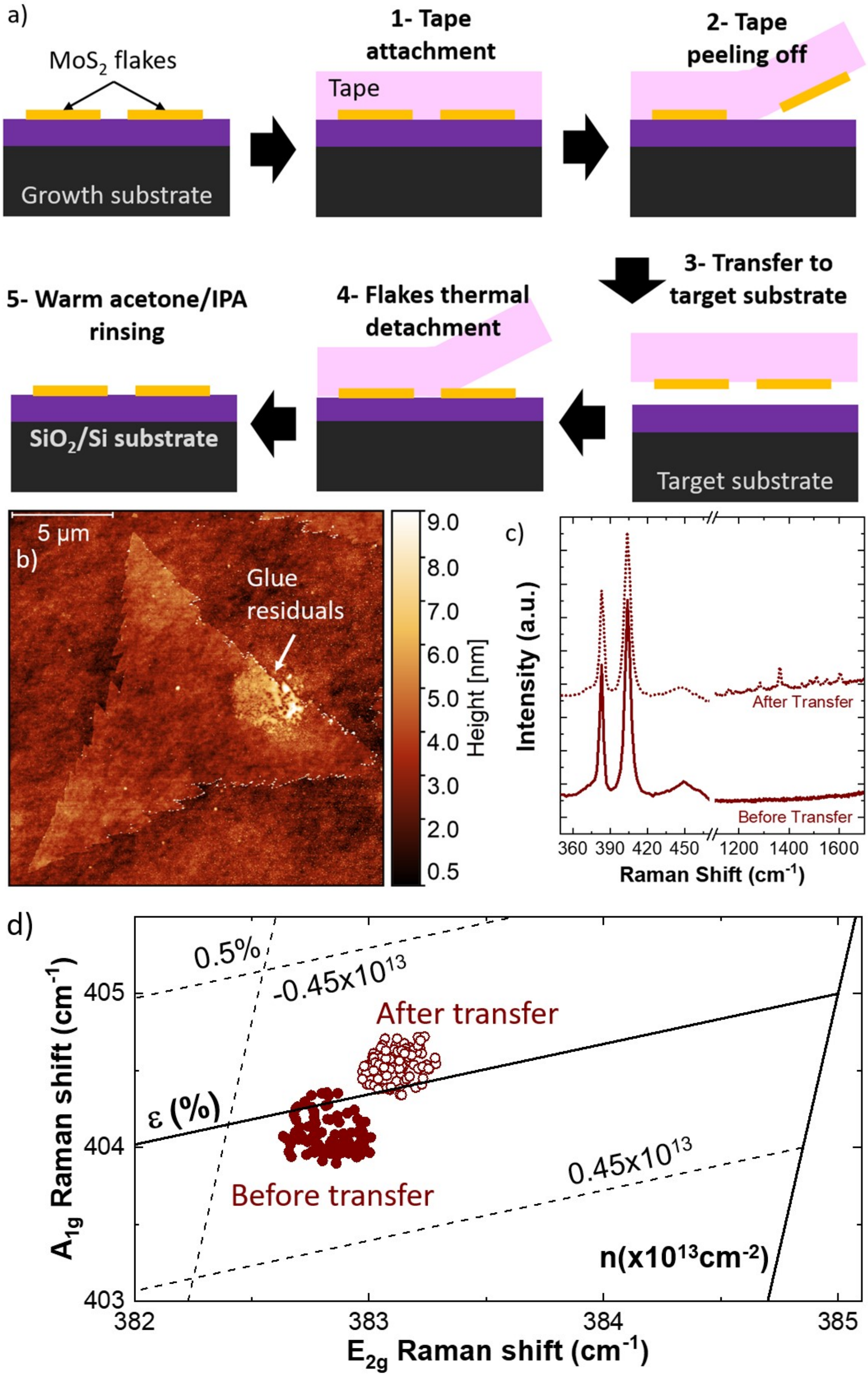

Figure S5. a) Graphical representation depicting the transfer process. b) AFM topological map of the MoS_2 ML, grown at 820°C, after the transfer. c) Representative Raman spectra before (full line) and after (dashed line) the transfer. d) MoS_2 doping/strain correlation plot, where the

full dots represent the data before the transfer while the open dots are acquired after the transfer.

In order to clarify the effect of the substrate on the built-in strain, we transfer the MoS_2 MLs, grown at 820°C. It is worth mentioning that the transfer of the 830°C synthetized MLs is hindered due to the presence of the nanocracks at the edge of the flakes. The transfer process is a modified dry viscoelastic stamping method[2–5], where the standard polydimethylsiloxane (PDMS) stamp is replaces with a polyethylene terephthalate (PET) tape with an acrylic adhesive. A similar approach has been widely employed in the transfer of graphene[6] and III-nitrides[7–9].

The transfer is based on different steps (Fig S5a). First, the PET tape is gently attached on the SiO_2/Si surface where the MoS_2 MLs are grown. Then the tape is peeled off very slowly and the MoS2 flakes remain attached to the tape. Then the tape is then attached on the acceptor surface, that in our case is a clean SiO_2/Si substrate. The specimen with the tape on tops is then annealed at 125°C in order to melt the acrylic adhesive and the tape is then gently peeled off, releasing the MoS_2 MLs on top of the new substrate. Then the specimen is rinsed in warm acetone and IPA for the removal of the acrylic adhesive residuals. This particular novel transfer method is developed because the standard transfer approach, employing the poly(methyl methacrylate) (PMMA) spin coating on the specimen surface, is hindered by presence of the byproduct nanoparticles on the edge of the flakes. The AFM topological map, Fig S5b, reports the presence of some areas of the flake affected by thick dhesive residuals, nevertheless a large part of the nanoparticles decorating the flakes edge are absent. The comparison of the Raman spectra before and after the transfer reveals that the appearance of different Raman modes in the 1000-1600 cm^{-1} range, related to the acrylic adhesive residuals (Fig. S5c).[10,11]

The analysis of the MoS_2 Raman modes (Fig.S5d), depicted in the A_{1g} versus E_{2g} Raman shift correlation plot, reveals that after the transfer process the strain is partially released in the MoS_2 ML, decreasing down to 0.35% and with a concurrent neutralization of the free carrier concentration. This second effect can be related to the presence of the adhesive residuals on the MoS_2 surface, as previously demonstrated in case of graphene.[12,13]

Figure S6: Topographical map of the MoS_2 ML affected by nanocracks.

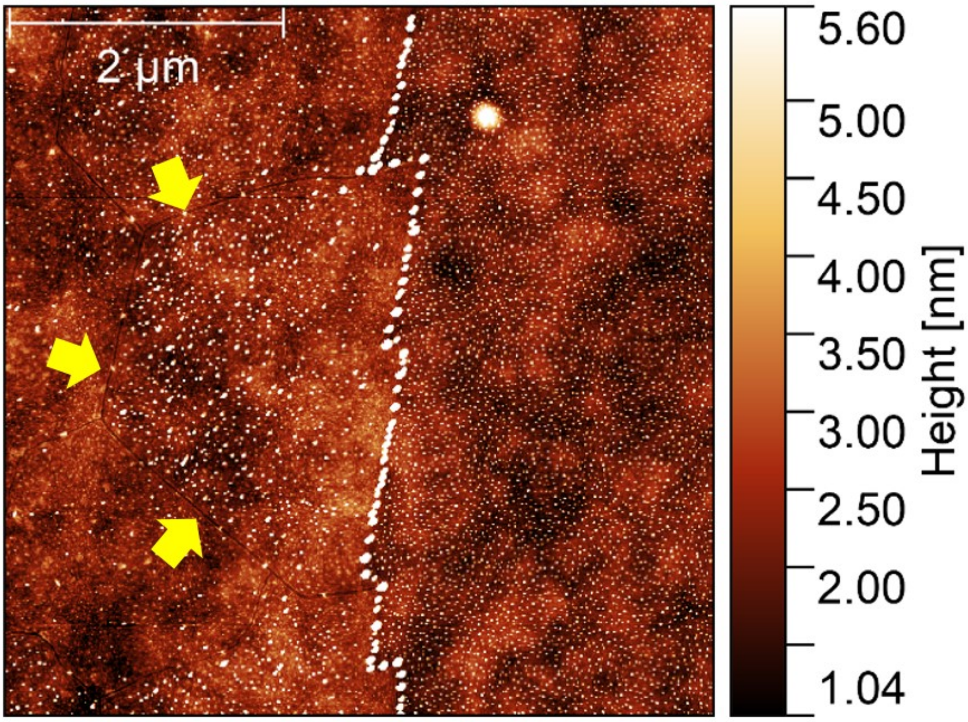

Fig. S6 Topological map of the MoS_2 ML area affected by nanocracks, indicated by yellow arrows.

The detection of the nanocracks in AFM topographic mode is hindered by the presence of the byproduct nanoparticles inside the MoS2 monolayer. The yellow arrows highlight the nanocracks reported in Fig. 4b.

Figure S6: Strain maps and AFM phase maps of the MoS$_2$ MLs grown at 810°C and 820°C.

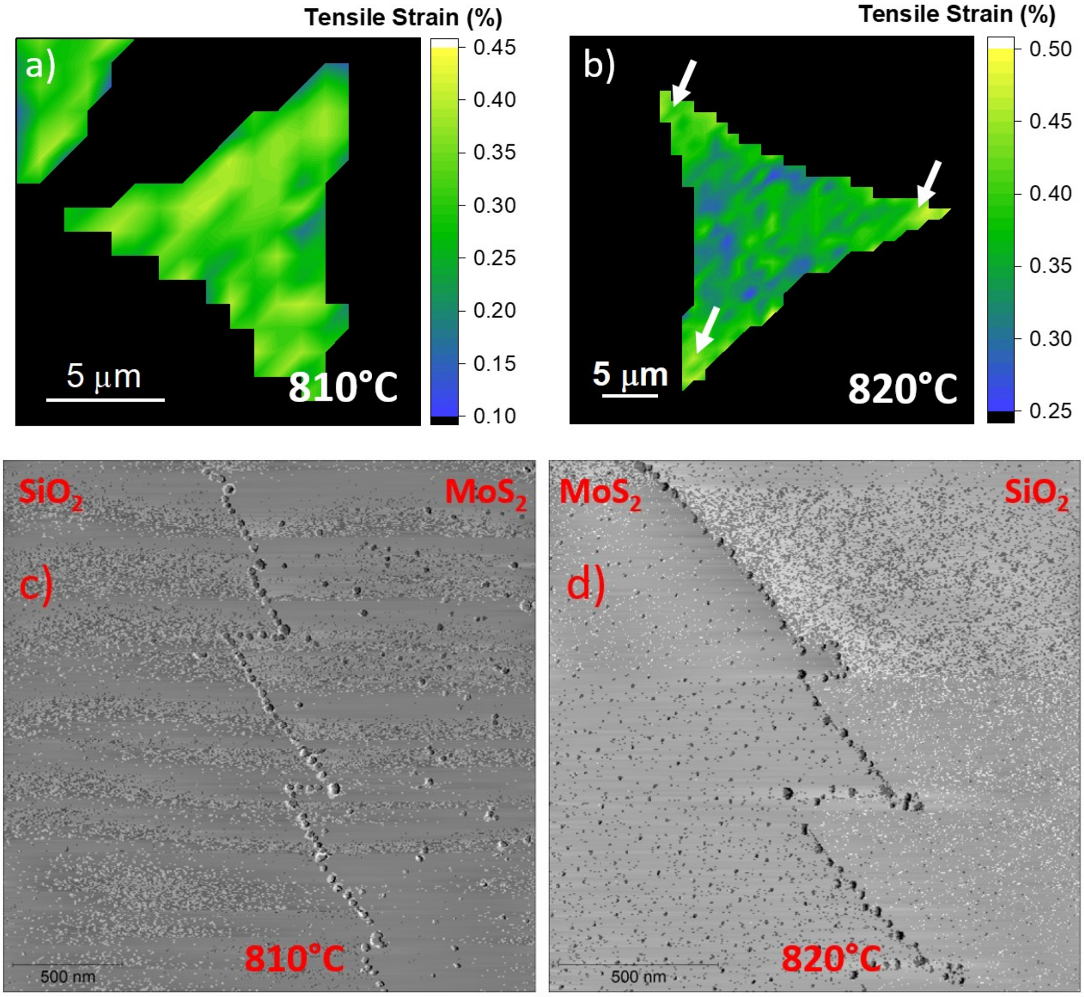

Fig. S7 a) and b) Strain map of the MoS$_2$ ML synthetized at 810°C and 820°C with the same color code reported in Fig. 4 of the manuscript. The white arrows indicate the increase of strain at the vertexes of the vertex sharp triangular flake. Fig. S5 c) and d) present the AFM phase maps of the ML synthetized at 810°C and 820°C.

The strain maps are obtained using the standard method proposed by A. Michail et al.[14,15]

$$\varepsilon = -\frac{\gamma(E^{'})Pos(E^{'})_0 i + \gamma(A_1{'})Pos(A_{1'})_0 j}{\sqrt{(\gamma(E^{'})Pos(E')_0)^2 + (\gamma(A_1^{'})Pos(A_1{'})_0)^2}}$$

The strain map (Fig S5a) of the MoS$_2$ ML grown at 810°C shows a tensile strain varying between 0.2% and 0.4%. In case of the MoS$_2$ ML grown at 820°C (Fig S6b), the strain map reveals that an increase of the tensile strain in the vertexes of the triangular monolayer, that reaches the maximum close to 0.5%, while in the body of the ML the tensile strain varies between 0.3% and 0.4%.

The AFM phase maps of the MoS_2 MLs synthetized at 810°C and 820°C are reported in Fig. S7 c) and d), respectively. The maps do not present the presence of nanocracks.

Figure S8: Comparison of PL spectra collected at the center and edge of the 830°C grown MoS_2 ML.

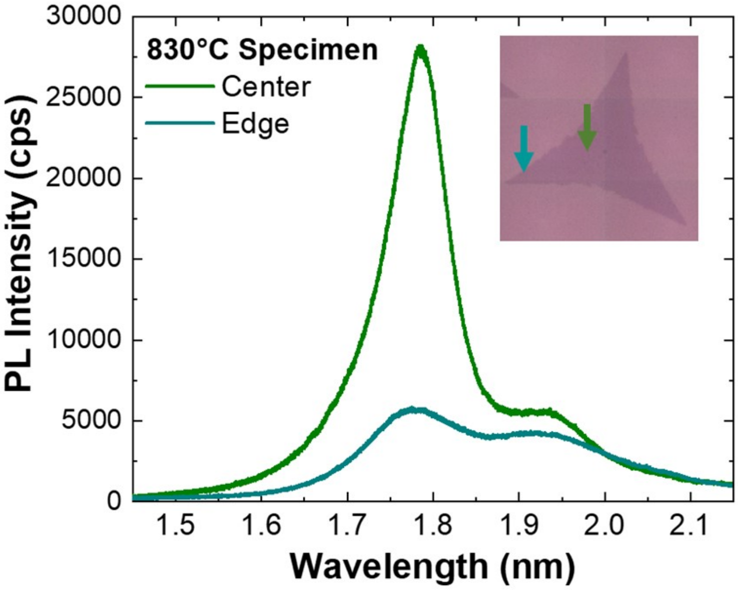

Fig. S8 PL spectra collected at the center (green line) and at the edge (dark cyan line) of the MoS2 ML grown at 830°C. The inset present the optical micrograph of the ML, where the colored arrows indicated the area of collection of the spectrum.

Fig. S8 reports the PL spectra obtained at the center (green line) and at the edge (dark cyan line) of the 830°C grown monolayer. The PL intensity of exciton A is drastically quenched due to the presence of non-radiative centers caused by the structural defects related to nanocracks.

Figure S9-S10: XPS characterization of Mo precursor solution spun on a SiO_2/Si substrate undergone a high temperature treatment at 830°C

We performed X-Ray Photoelectron Spectroscopy (XPS) on the Mo precursor solution spunned on SiO_2/Si substrate after a high temperature treatment at 830°C to identify the surface chemical state of the compounds formed during such treatment. As a reference, we analyzed Na_2SiO_3 pure powder, purchased from Sigma-Aldrich, Merck Life Science S.r.l.. Despite the formation of Na_2MoO_4 is cited as possible reaction product between MoO_3 and NaOH at high temperature[16], we do not detect any evidence of sodium molybdate from XPS. Na_2MoO_4 pure powder was analyzed for reference in the same UHV apparatus and compared to results from the treated surface ("Mo precursor solution" sample), but lineshape analysis is not consistent with this compound.

Long range spectrum of the treated substrate (Fig. S7, black curve) shows the presence of sodium (Na1s), oxygen (O1s), carbon (C1s), molybdenum (Mo3d), and silicon (Si2p). Mo3d core levels revealed the presence of two doublets (Mo3d 5/2, 3/2 due to spin orbit coupling) located at 232.2-235.3eV and 230.4-233.5eV, related to MoO_3 and MoO_2 molybdenum oxides (Fig. S8a)[17,18]. Si2p shows a main feature at 103.5 eV, due to SiO_2 and a minor component at 102.5 eV, that is consistent with the presence of Na_2SiO_3 (Figure S8b) and S8c), bottom curves). The Na/Si ratio is 2.1±0.05 and Na1s-Si2p energy difference is 969.4 eV (Na1s is located at 1072.1 eV), in good agreement with the results of sodium silicate analyzed as reference.

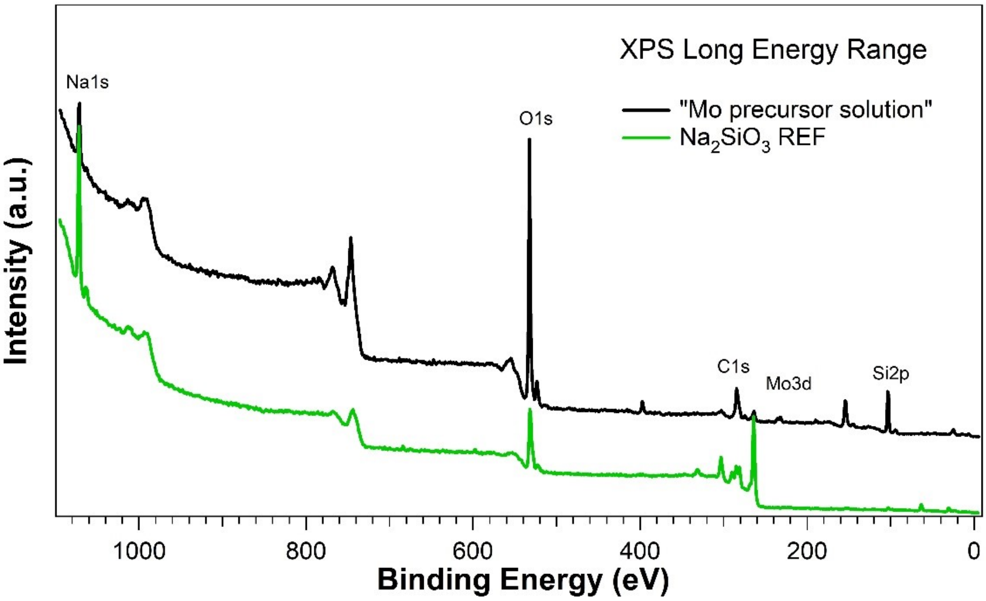

Fig. S9: Long range XPS spectra of the Mo precursor solution on SiO_2 surface after a treatment at 830°C (black curve), and pure Na_2SiO_3 for reference (green curve).

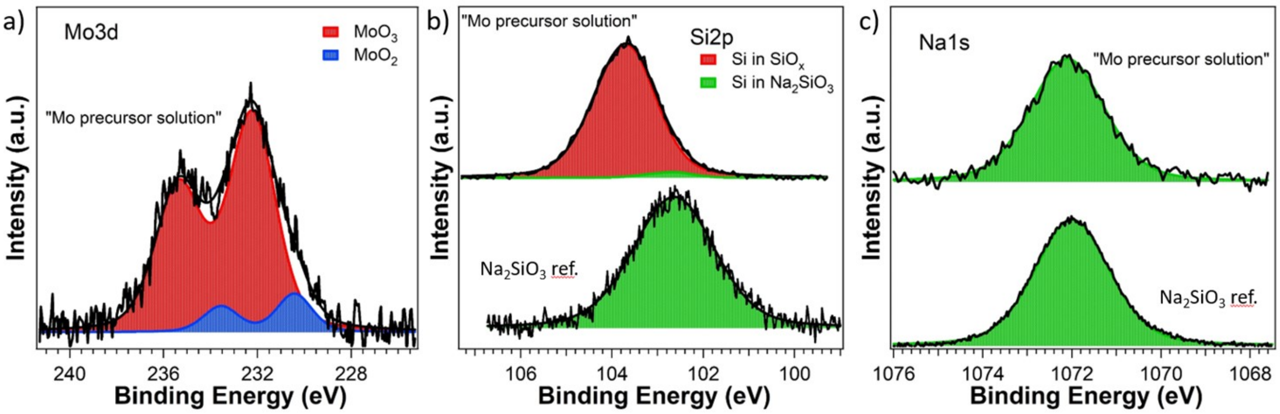

Fig. S10 XPS core level spectra of Mo3d a), Na1s b), and Si2p c) of the Mo precursor solution on SiO$_2$ surface after a treatment at 830°C. In b) and c), the corresponding core levels of pure Na$_2$SiO$_3$ are shown for reference (bottom curves). Spectra are normalized in height.

Figure S11: Schematic illustration of the CVD reactor.

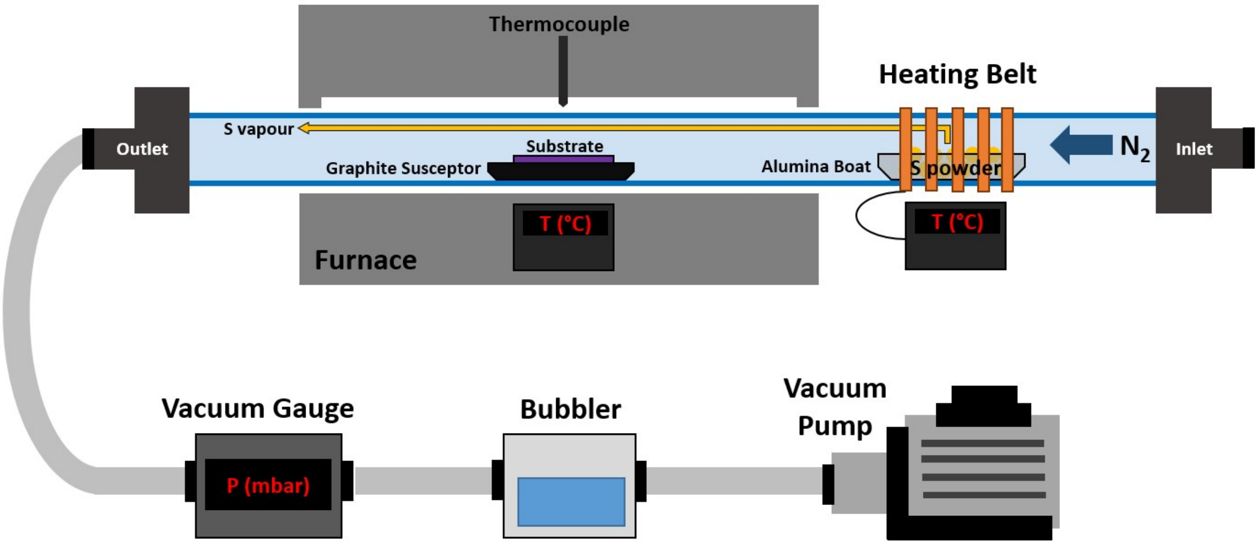

Fig. S11 Schematic illustration of the CVD reactor, employed in this work.

The schematic illustration of the CVD reactor is shown in Fig. S10. The low temperature zone is heated up using a heating belt to reach the desired temperature. The sulfur powder is placed on an alumina boat while the growth substrate, where the Mo precursor solution is spun, is positioned on a graphite susceptor for a uniform heating.

References

1 M. Macha, H. G. Ji, M. Tripathi, Y. Zhao, M. Thakur, J. Zhan, A. Kis and A. Radenovic, *Nanoscale Adv.*, , DOI:10.1039/D2NA00409G.

2 M. A. Meitl, Z.-T. Zhu, V. Kumar, K. J. Lee, X. Feng, Y. Y. Huang, I. Adesida, R. G. Nuzzo and J. A. Rogers, *Nat. Mater.*, 2006, **5**, 33–38.

3 A. Castellanos-Gomez, M. Buscema, R. Molenaar, V. Singh, L. Janssen, H. S. J. van der Zant and G. A. Steele, *2D Mater.*, 2014, **1**, 11002.

4 R. A. Hemnani, J. P. Tischler, C. Carfano, R. Maiti, M. H. Tahersima, L. Bartels, R. Agarwal and V. J. Sorger, *2D Mater.*, 2019, **6**, 15006.

5 A. Portone, L. Bellucci, D. Convertino, F. Mezzadri, G. Piccinini, M. A. Giambra, V. Miseikis, F. Rossi, C. Coletti and F. Fabbri, *Nanoscale Adv.*, 2021, **3**, 1352–1361.

6 X.-D. Chen, Z.-B. Liu, C.-Y. Zheng, F. Xing, X.-Q. Yan, Y. Chen and J.-G. Tian, *Carbon N. Y.*, 2013, **56**, 271–278.

7 E. W. Blanton, M. J. Motala, T. A. Prusnick, A. Hilton, J. L. Brown, A. Bhattacharyya, S. Krishnamoorthy, K. Leedy, N. R. Glavin and M. Snure, *Small*, 2021, **17**, 2102668.

8 W. Song, Q. Chen, K. Yang, M. Liang, X. Yi, J. Wang, J. Li and Z. Liu, *Adv. Funct. Mater.*, 2023, **33**, 2209880.

9 Y. Jia, H. Wu, J. Zhao, H. Guo, Y. Zeng, B. Wang, C. Zhang, Y. Zhang, J. Ning, J. Zhang, T. Zhang, D. Wang and Y. Hao, *CrystEngComm*, 2021, **23**, 7406–7411.

10 J. Chen, Y. Huang, P. Kannan, L. Zhang, Z. Lin, J. Zhang, T. Chen and L. Guo, *Anal. Chem.*, 2016, **88**, 2149–2155.

11 F. J. Boerio, P. P. Hong, P. J. Clark and Y. Okamoto, *Langmuir*, 1990, **6**, 721–727.

12 C. Deng, W. Lin, G. Agnus, D. Dragoe, D. Pierucci, A. Ouerghi, S. Eimer, I. Barisic, D. Ravelosona, C. Chappert and W. Zhao, *J. Phys. Chem. C*, 2014, **118**, 13890–13897.

13 X. Yang and M. Yan, *Nano Res.*, 2020, **13**, 599–610.

14 A. Michail, N. Delikoukos, J. Parthenios, C. Galiotis and K. Papagelis, *Appl. Phys. Lett.*, 2016, **108**, 173102.

15 A. Michail, D. Anestopoulos, N. Delikoukos, J. Parthenios, S. Grammatikopoulos, S. A. Tsirkas, N. N. Lathiotakis, O. Frank, K. Filintoglou and K. Papagelis, *2D Mater.*, 2020, **8**, 15023.

16 H. Kim, G. H. Han, S. J. Yun, J. Zhao, D. H. Keum, H. Y. Jeong, T. H. Ly, Y. Jin, J. H. Park, B. H. Moon, S. W. Kim and Y. H. Lee, *Nanotechnology*, , DOI:10.1088/1361-6528/aa7e5e.

17 J.-C. Dupin, D. Gonbeau, P. Vinatier and A. Levasseur, *Phys. Chem. Chem. Phys.*, 2000, **2**,

1319–1324.

18 W. Swartz and D. M. Hercules, *Anal. Chem.*, 1971, **43**, 1774–1779.